CLARET: A Fast Deformable Registration Method Applied to Lung Radiation Therapy

Chen-Rui Chou[1], Brandon Frederick[2], Xiaoxiao Liu[4], Gig Mageras[5], Sha Chang[2,3], Stephen Pizer[1,2,3]

[1] Dept. of Computer Science, University of North Carolina at Chapel Hill, NC
[2] Dept. of Biomedical Engineering, University of North Carolina at Chapel Hill, NC
[3] Dept. of Radiation Oncology, University of North Carolina at Chapel Hill, NC
[4] Kitware, Inc., Clifton Park, NY
[5] Dept. of Medical Physics, Memorial Sloan-Kettering Cancer Center, New York, NY

Abstract. We present a novel 3D-to-2D registration method called CLARET (Correction via Limited-Angle Residues in External Beam Therapy) that has potential application to rapid and accurate image-guided radiotherapy in lung with low-dose imaging. CLARET contains three components: shape modeling, machine learning of regression matrices, and treatment application. It models the patient's breathing space from the patient's treatment planning Respiratory-Correlated CTs (RCCTs) through an Large Deformation Diffeomorphic Metric Mapping (LDDMM) / Principal Component Analysis (PCA) framework. The eigenmode weights form the 3D shape parameters. Second, it performs multi-scale linear regressions between selected 3D shape parameters and covariates defined by intensity residues in the 2D projection space. At treatment time, CLARET computes a patient's lung deformations by iteratively applying the learned regression matrices on the normalized intensity residues between the treatment-time imaging radiographs and corresponding projections of the current estimated CT. Both our synthetic and clinical test results show that CLARET can provide fast and accurate treatment-time 3D shape deformation corrections using a single radiograph for Image-Guided Radiation Therapy (IGRT).

1 Introduction

Recent advances in Image-Guided Radiation Therapy (IGRT) emphasize the capability of fast treatment-time tumor localization while using low imaging radiation dose. A 3D/2D registration framework has shown promise for lung IGRT: With the patient's respiratory motion model computed, the patient's treatment-time lung deformations can be calculated by iteratively matching the Digitally-Reconstructed Radiographs (DRRs) of the deformed CT to the treatment-time radiographs with a regularization to the model space. Long *et al.* and Brock *et al.* used cubic B-splines as the respiratory motion model in this framework and showed accurate estimations of the treatment-time Deformation Vector Fields (DVFs) by using limited-angle radiographs [1] and a small number of radiographs [2] respectively. Li *et al.* [3,4] extended this 3D/2D framework and built

the respiratory motion model by doing Principal Component Analysis (PCA) on the 4D Respiratory-Correlated CTs (RCCTs) acquired at treatment simulation. They used a GPU-accelerated gradient-descent optimization scheme that showed accurate tumor localization with a single radiograph.

However, traditional gradient descent optimization approaches suffer from complexity in computing the image Jacobian, and they also require a well-defined convex metric to guarantee that the scheme reaches the global optimum.

Chou *et al.* [5] instead used a novel regression-based matching scheme in this 3D/2D framework for patient re-positioning in head-and-neck IGRT. Referred to as CLARET (Correction via Limited-Angle Residues in External Beam Therapy), it parameterized the patient's rigid motion and performed regression learning on the intensity residues between the DRRs of the transformed CT and the treatment-time radiographs. For the treatment application, their 3D/2D image registration can be accomplished in real time by computationally inexpensive matrix multiplications.

In this paper, we adapt CLARET to radiotherapy of lung tumors by introducing the following enhancements: 1) We extend the theoretically fast regression-based 3D/2D image matching in [5] to deformable registrations in lung. 2) We build an improved respiratory motion model using a Large Deformation Diffeomorphic Metric Mapping (LDDMM) between a Fréchet mean image and each phase-binned CT in the RCCT set. A principal component analysis (PCA) is applied to the resultant Displacement Vector Fields (DVF) to derive the motion model. 3) We adapt a local Gaussian normalization scheme [6] for removal of x-ray scatter from radiographs, followed by a histogram matching scheme for intensity correction between the DRRs and the radiographs.

The rest of the paper is organized as follows: In Sections 2, 3, and 4 we describe each component of the CLARET method - shape modeling, machine learning and the treatment application respectively. In Section 5 we present results on the accuracy of CLARET - as a function of the number and angular spacing of the radiographs. We conclude this paper and discuss future work in Section 6.

2 Shape Modeling

CLARET uses a patient-specific lung motion modeling. It models the patient's breathing space with the patient's planning 4D RCCT in two steps: 1) Calculation of a Fréchet mean and diffeomorphisms from it for the respiration phases; 2) PCA statistical analysis of the DVFs to model the patient's breathing manifold.

2.1 Breathing Manifold Generation

In order to model the breathing space realistically, CLARET computes the patient's respiratory intrinsic mean by Fréchet mean image $\overline{I}$ via an LDDMM framework on the individual within-phase CTs making up the N - phase RCCT.

The Fréchet mean, as well as diffeomorphic displacement maps from the mean to each phase image, are computed using a fluid-flow distance metric [7] :

$$\overline{I} = \underset{I}{argmin} \sum_{i=1}^{N} d(I, I_i)^2 = min \int_0^1 \int_\Omega ||v(x)||^2 dx dt + \frac{1}{\sigma^2} \int_\Omega ||I(\phi^{-1}(x)) - I_i(x)||^2 dx, \tag{1}$$

where $I_i(x)$ is the intensity of the pixel at position x in the i^{th} image of the RCCT set, v is the fluid-flow velocity field with time t, σ is the weighting variable on the image dissimilarity, and $\phi(x)$ describes the deformation of the pixel at location x: $\phi(x) = x + \int_0^1 v(x)dt$.

The Fréchet mean image and the corresponding DVF to the i^{th} phase RCCT, ϕ_i, is calculated by gradient descent optimization. They can be used to generate the breathing manifold by the following statistical analysis. See an example Fréchet mean image in Figure 1(c).

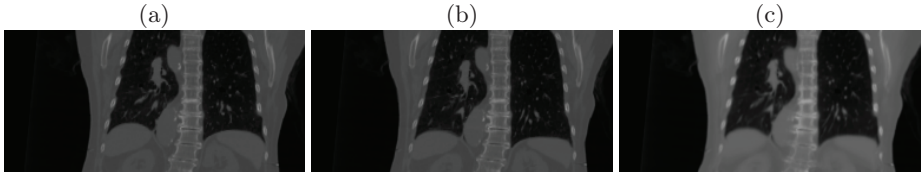

Fig. 1. A patient's (a) planning CT at the End-Expiration (EE) phase, (b) planning CT at the End-Inspiration (EI) phase and (c) respiratory Fréchet mean CT generated via an LDDMM framework.

2.2 Statistical Analysis

CLARET calculates the principal modes of deformation variation by doing PCA on the N DVFs, $\phi_1 ... \phi_N$, computed in the previous step.

We have found that 2 - 3 modes of variation suffice to obtain 95% of the total variation. See Figure 2 for the visualization of the principal DVFs of a lung dataset. Based on verification that can be found in [8] , we assume that the patient's time-varying deformations of the lung at treatment time, ϕ_t, can be spanned by these eigenmodes, ϕ_{pc}, with weighting parameters λ and the mean DVF, $\overline{\phi}$.

$$\phi_t = \overline{\phi} + \sum_i \lambda_t \cdot \phi_{pc}^i$$

However, the values of the eigenmode weights through a respiratory cycle need not be the same as at planning time. CLARET's objective at treatment time is to find the eigenmode weights and thus the Fréchet mean diffeomorphisms that correspond to the images at treatment time.

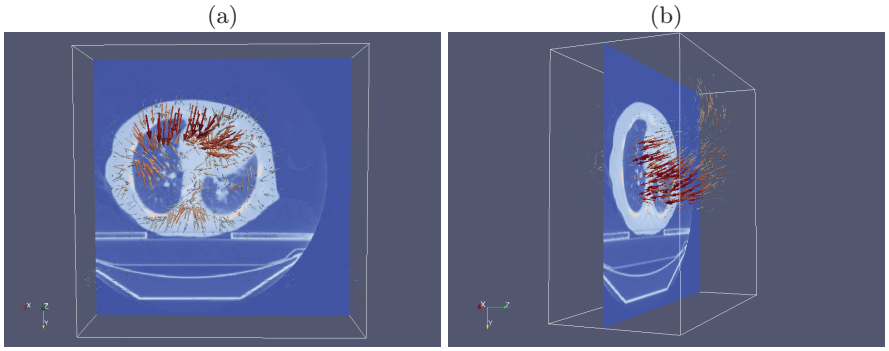

Fig. 2. The (a) first and (b) second principal components of DVFs analyzed from the RCCTs of a lung dataset. Colored lines indicate heat maps of the DVF magnitudes. As shown in the images, the first principal motion is the expansion / shrinkage of the lung and the second principal motion is along SI direction. $\overrightarrow{X}$: Left to Right (LR); $\overrightarrow{Y}$: Anterior to Posterior (AP); $\overrightarrow{Z}$: Superior to Inferior (SI).

3 Machine Learning

CLARET needs to learn how to transform the image data into eigenmode weights. It does this using a regression approach similar to that used in Active Appearance Models [9]. The regression matrix describes the best linear transformation on 2D intensity residues to give eigenmode weights. The intensity residues are produced by concatenating pixel-wise intensity differences in the DRRs at different respiratory shapes. DRRs are generated by a GPU-based CT volume re-projection function, P.

3.1 Residues to Eigenmode Weights Regression

We adapt a machine learning method initiated in [5] that uses linear regression to correlate the eigenmode weighting parameters λ_j in the j^{th} training case with the covariated intensity residues between the concatenation of the n DRRs at the deformed and mean patient motion states. n is the number of DRRs simulated from a limited angular range that corresponds to the treatment-time imaging geometry.

$$\lambda_j = [P(\overline{I} \circ \phi_j) - P(\overline{I})]^n \cdot M,$$

where M is the regression matrix that will be applied in the treatment stage to yield the estimated eigenmode weights λ.

However, it is unrealizable to enumerate many combinations in λ. Therefore, we use the multiscale piecewise approximation scheme described in the next section.

3.2 Multiscale Training

In the training stage, K multiscale regression matrices $M_1,\ M_2, \cdots,\ M_K$ are generated from large to small scales of training. At the k-th level of training, the eigenmode weights λ are collected from the combinations of $\pm\lambda_k$ and 0. In order to have accurate estimations in the whole training domain, the selection of λ_k depends on the interpolation accuracy of M_k such that the union of each level's confidence interval, τ_λ^k , covers the whole training domain.

$$\bigcup_{k=1}^{K} \tau_\lambda^k \supseteq [-\lambda_{limit},\ \lambda_{limit}],$$

where $\pm\lambda_{limit}$ is the training limits for the parametrized transformation. In this paper, we took 3 standard deviation of the DVFs in the RCCTs as the limits of our training.

In the treatment stage the calculated multiscale regression matrices are applied sequentially, from M_1 to M_K , to give new deformation combinations when CLARET fails to decrease the Sum of the Squared Difference (SSD) between the DRRs at the estimated shape and the radiographs. In this paper, we applied four scales ($K = 4$) with $\lambda_k = (K - k + 1) \cdot \lambda_{limit}/K$.

4 Treatment Application

4.1 Local Gaussian Normalization and Histogram Matching

CLARET's regression learning requires comparable intensities between the 2D DRRs and the radiographs J to have adequate registration quality. However, the x-ray scattering artifacts in the treatment-time radiographs will impose incomparable intensities. Therefore, CLARET uses a localized Gaussian normalization method described in [6] that will remove the undesired scattering artifacts. This localized Gaussian normalization together with the histogram matching scheme described below is intended to produce intensity consistent radiographs.

For each Gaussian window, CLARET calculates the local mean $\overline{u}$ and standard deviation σ and normalizes the intensity for each pixel u in the window:

$$\hat{u} = \frac{u - \overline{u}}{\sigma}, \text{ where } \hat{u} \text{ is the normalized intensity.}$$

In this paper, we use a Gaussian window with an RMS width of 31.98 mm where CLARET yields the most accurate 3D tumor localization. See Figure 5.

Also, in order to correct the intensity spectrum differences between the DRRs $P(\overline{I})$ at the mean shape and the locally normalized / estimated scatter removed radiographs $\tilde{J}$, a function F on intensity achieving non-linear cumulative histogram matching is applied in CLARET after normalization. That is, F is defined by

$$F(H_f(\tilde{J})) = H_f(P(\overline{I})),$$

where H_f is the culmulative histogram profiling function for the lung region in the images. In this paper, we used the mean intensity to threshold the lung region. The histogram matched intensities $\hat{J}$ can be calculated through the mapping: $\hat{J} = \tilde{J} \circ F$. See the illustration in Figure 3.

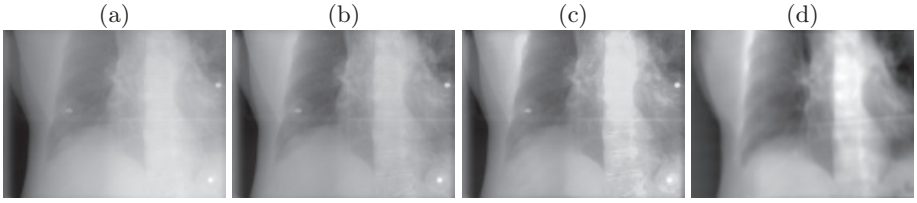

Fig. 3. A patient's (a) raw Cone-Beam (CB) radiograph, (b) local Gaussian normalized CB radiograph, (c) histogram matched CB radiograph at the EE phase and (d) DRR at the mean respiratory phase at angle =14.18°. As shown in the images, after normalization and histogram matching, the intensity contrast in the radiograph becomes closer to that in the DRR.

4.2 Iterative Matching

After normalization and histogram matching for the treatment-time radiograph, CLARET calculates the intensity residues between the DRRs at the mean shape and the normalized radiographs $\hat{J}$. It then applies the learned multiscale regression matrices M in sequence to yield the estimated eigenmode weights λ. The estimated CT is generated by deforming the Fréchet mean CT $\bar{I}$ with the estimated eigenmode weights λ and the eigenmode DVFs ϕ_{pc}. The estimated CT is then used in the next iteration to generate the DRRs at the updated shape. The iterative process stops when the SSD of intensity between the radiographs and the estimated DRRs is below the threshold thr. DRRs are generated in real-time with GPU acceleration. As shown in Section 5, equipping this iterative scheme with the multiscale training and application, CLARET can estimate the lung deformation, ϕ', accurately. See Algorithm 1 for the detailed iterative matching scheme.

5 Results

We tested CLARET's deformable registration with 1) the 4D non-uniform rational B-spline (NURBS) based cardiac-torso (NCAT) phantom data in Section 5.1 and b) synthetic and real patient data in Section 5.2.

5.1 NCAT Phantom Data

4D NCAT phantom thorax CTs (CT dimension: $512 \times 512 \times 200$; voxel size: 2.23 mm) were produced [10] at 10 phases sampled in one breathing cycle. These were

Algorithm 1 The CLARET's treatment-time application algorithm.

Input:
$\bar{I}$: Fréchet mean CT;
$\bar{\phi}$: Mean DVF;
ϕ_{pc}: Eigenmode DVFs;
M: Regression matrices;
thr: SSD threshold value;
Output:
I': Estimated CT;
ϕ': Estimated DVF;
foreach *Acquisition of treatment-time radiographs* J **do**
  SSD =MAX_NUMBER;
  $I' = \bar{I}$;
  $\hat{J}$ =LGN_HM(J,$P(\bar{I})$); //Local Gaussian Normalization and Histogram Matching
  foreach *k^{th} scale of regression matrix application* **do**
    while $SSD \geq thr$ **do**
      $\lambda = [\hat{J} - P(I')] \cdot M_k$;
      $\phi' = \bar{\phi} + \sum_i \lambda \cdot \phi^i_{pc}$;
      $I' = \bar{I} \circ \phi'$;
      $SSD = ||\hat{J} - P(I')||$;
    end
  end
end

used as the treatment planning CTs to produce the respiratory shape space. A corresponding CBCT sequence was simulated at 6 phases from the NCAT CTs using the protocol of a gantry-mounted kV on-board imaging system (Varian Medical Systems) used in the clinical IGRT setup. The DRRs of the simulated CBCT phases were generated as the simulated target radiographs. In this NCAT test, CLARET registered the Fréchet mean CT of the 4D thorax CTs to the 5 simulated coronal radiographs 5 degrees apart in total ($-2.5°$to $2.5°$). The registration quality was then validated by measuring the tumor's 3D Center Of Gravity (CoG) difference between the CLARET-estimated CT and the CBCT at the target phase. 3D tumor CoGs were calulated from their active contour (Snake) segmentations [11]. As shown in Table 1, CLARET yields sub-voxel accuracy at all CBCT phases except phase 5, where the error is 1.25 voxels.

CBCT phase number	1	2	3	4	5	6
Before registration	3.94	1.51	4.81	5.63	2.79	2.32
After registration	1.77	1.51	2.20	1.14	2.79	1.44

Table 1. 3D tumor CoG error (mm) before and after CLARET's registration for the 6 NCAT-simulated CBCT phases.

5.2 Patient Data

Respiratory-correlated CT (RCCT) data sets (CT dimension: $512 \times 512 \times 120$; voxel size: 2.28 mm) were generated by a 8-slice scanner (LightSpeed i, GE Medical Systems), acquiring repeat CT images for a complete respiratory cycle at each couch position while recording patient respiration (Real-time Position Management System, Varian Medical Systems). The CT projections were retrospectively sorted (GE Advantage 4D) to produce 3D images at 10 different respiratory phases.

In the following sections, we demonstrate CLARET's registration results on both synthetic and real patient CB radiographs.

Synthetic Treatment Radiographs We used the DRRs of the target CTs as the synthetic treatment-time radiographs. The DRRs were generated to simulate radiographs in a gantry-mounted kV on-board imaging system (Varian Medical Systems). The target CTs were deformed from the patient's Fréchet mean CT by taking normally distributed random samples of the coefficients of the first three eigenmodes of the DVFs of the patient's RCCTs.

For each one of the 10 CLARET's registrations, we used a *single* simulated coronal radiograph (dimension: 128×96; pixel spacing: 3.10 mm) at angle $= 14.18°$ (see Figure 3(d)) as the input. The registration quality was then validated by measuring the 3D tumor CoG (again via Snake segmentations) difference between the CLARET-estimated CT and the target CT. As shown in Table 2, after registration CLARET can reduce more than 85% of CoG error.

Test cases	1	2	3	4	5	6	7	8	9	10
Before registration	8.23	21.33	21.78	20.05	9.86	10.24	10.92	15.72	14.87	19.91
After registration	1.30	0.78	1.52	3.33	0.75	1.31	0.45	1.57	2.07	2.72

Table 2. 3D tumor CoG error (mm) before and after CLARET's registration for the 10 randomly generated test cases.

We studied CLARET's registration quality in average DVF error per CT voxel versus different angular spacings for training. For each sampling angle, we generated 30 random test cases as described in the previous section. Figure 4(a) shows the DVF error reduces with appropriately large angular spacings.

We also studied CLARET's registration quality in average DVF error per CT voxel versus the number of DRRs used for training. For each number of DRRs, we generated 30 random test cases as described in the previous section. Figure 4(b) shows no particular trend.

As a result, we used a single radiograph to test CLARET's registration for the real patient data in the next section.

Real Treatment Radiographs We tested CLARET on 5 lung cancer paitents' data with the on-board CBCT system mentioned before. CBCT radiographs were shifted 16 cm to the left for acquiring CBCT scans in a half-fan mode.

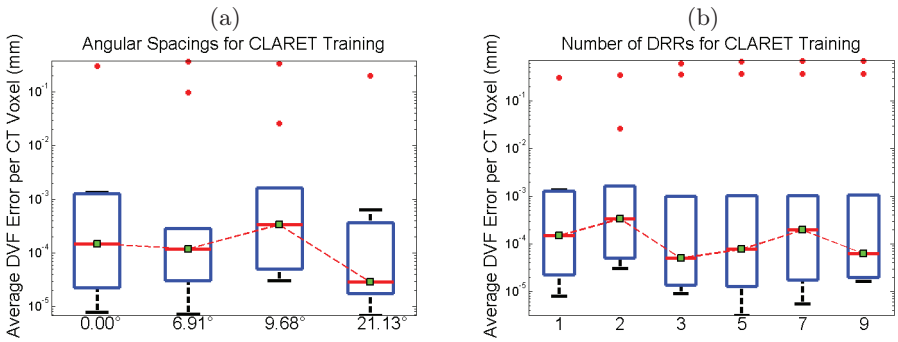

Fig. 4. Boxplot results of CLARET errors in (a) the angular spacing study and (b) the number of DRRs used for inputs. Red dots are the outliers. In (a), two DRRs for each test were used. For the zero-degree test case, only one DRR was used. In (b), DRRs spanning 9.68° about 14.18° were used in each test. For the single DRR test case, it was tested at angle = 14.18° (see Figure 3(d)).

In this real patient study, a *single* coronal on-board CB radiograph (dimension: 1024×768; pixel spacing: 0.388 mm) downsampled to dimension: 128×96 with pixel spacing: 3.10 mm at 14.18° (see Figure 3(a)) at both the EE and the EI phases were used for CLARET's testing. We measured the 3D tumor CoG (see Figure 6(a)) difference between the CLARET-estimated CT and the reconstructed CBCT at the same respiratory phase as the testing radiograph. For the Gaussian normalization, we set the RMS width of the Gaussian window to 31.98 mm for this imaging geometry where CLARET yielded the smallest 3D CoG error for a lung dataset (see Figure 5). The results shown in Table 3 suggest a consistency of registration quality between the synthetic tests and the real patient tests. The average computation time is 5 seconds with a laptop GPU. The largest contribution to the difference is in the direction perpendicular to the radiograph plane (see the difference along the AP direction in Figure 6(b)), which is expected because the CoG in that direction is determined from apparent tumor size. For directions in the radiograph plane, CLARET can accurately locate the tumor. See Figure 7.

Patient#	EE, initial	EE, after CLARET	EI, initial	EI, after CLARET
1	7.96	2.27	8.03	5.26
2	9.70	3.20	7.45	2.85
3	1.50	1.32	3.59	2.03
4	10.17	2.77	5.53	2.31
5	3.52	2.24	3.89	2.40

Table 3. 3D CoG error (mm) of EE and EI phases before and after CLARET's registration for 5 patients' on-board CBCT data set.

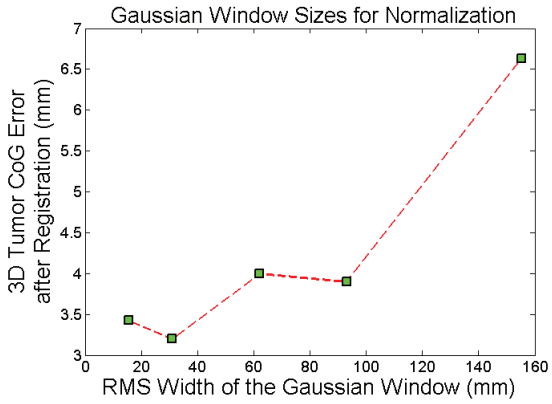

Fig. 5. 3D tumor CoG error plots on a lung dataset with varying sizes of the Gaussian window used for CLARET's local Gaussian normalization.

Visual Validation Figure 6 (b) shows the 3D meshes of the tumors in the mean CT, the CBCT at EE respiratory phase, and the estimated CT of a lung dataset for visual validation. As shown in the figure, CLARET moves the tumor up in the lung from the mean image; this is theoretically at EE phase. Figure 7 shows the corresponding coronal slices of the mean CT, the reconstructed CBCT at the EE phase and the estimated CT of the same lung dataset. As shown in Figure 7, CLARET can accurately locate the tumor in the radiograph plane (coronal plane).

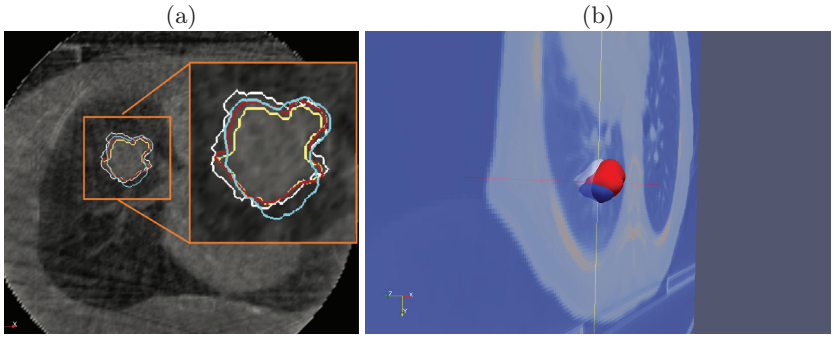

Fig. 6. (a) Manual segmented contours in the reconstructed CBCT at specific phase. They were used for 3D CoG calculation. (b) Tumor meshes in the mean CT (gray), in the CBCT at the EE respiratory phase (blue) and in the estimated CT (red). $\overrightarrow{X}$: Left to Right; $\overrightarrow{Y}$: Anterior to Posterior; $\overrightarrow{Z}$: Superior to Inferior.

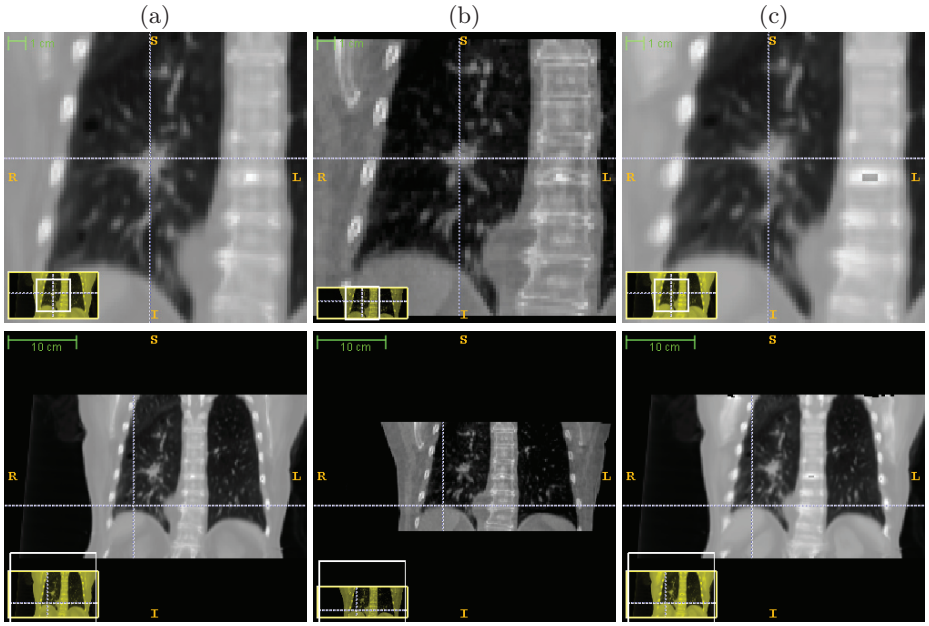

Fig. 7. Corresponding lines in the same coronal slices of (a) the mean CT, (b) the reconstructed CBCT at the EE phase and (c) the estimated CT of the same lung dataset used in Figure 6(b). Upper row: lines locating the tumor CoG in the CBCT at the EE phase; lower row: lines locating the diaphragm contour in the CBCT at the EE phase.

6 Conclusions and Discussion

We presented a novel deformable 3D/2D registration method - CLARET that estimates 3D DVF eigenmode coefficients using patient-specific machine learning of a regression with 2D radiographs. The synthetic and real test results have shown CLARET's promise to provide fast and accurate tumor localization with a single treatment-time imaging radiograph for IGRT. The future work of CLARET will be 1) to reduce the uncertainty in direction perpendicular to the radiograph plane by including a second radiograph in the fit at an oblique angle to the first and 2) to extend the current respiratory space modeling to include the treatment-time possible variations that are not in the prior RCCT space. This will allow CLARET to correct patient's respiratory motions more comprehensively.

7 Acknowledgements

The authors would like to thank Lei Pan, Dr. Michael Lawrence and Dr. David Lalush for the fruitful discussion on the development of CLARET.

References

1. Y, L., JA, F., JM, B.: Accuracy estimation for projection-to-volume targeting during rotational therapy: a feasibility study. Medical Physics **37** (2010) 2480–2490
2. Brock RS, Docef A, M.M.: Reconstruction of a cone-beam ct image via forward iterative projection matching. Medical Physics **37** (2010) 6212–6220
3. Li, R., Jia, X., Lewis, J.H., Gu, X., Folkerts, M., Men, C., Jiang, S.B.: Real-time volumetric image reconstruction and 3d tumor localization based on a single x-ray projection image for lung cancer radiotherapy. Medical Physics **37** (2010) 2822–2826
4. Li, R., Lewis, J.H., Jia, X., Gu, X., Folkerts, M., Men, C., Song, W.Y., Jiang, S.B.: 3d tumor localization through real-time volumetric x-ray imaging for lung cancer radiotherapy. Medical Physics **38** (2011) 2783–2794
5. Chou, C., Frederick, C., Chang, S., Pizer, S.: A Learning-Based patient repositioning method from Limited-Angle projections. In: Brain, Body and Machine. Volume 83 of Advances in Soft Computing. Springer Berlin / Heidelberg (2010) 83–94
6. Cachier, P., Pennec, X.: 3d non-rigid registration by gradient descent on a gaussian-windowed similarity measure using convolutions. In: Mathematical Methods in Biomedical Image Analysis, 2000. Proceedings. IEEE Workshop on. (2000) 182 –189
7. Davis, B.C., Bullitt, E., Fletcher, P.T., Joshi, S.: S.: Population shape regression from random design data. In: In: Proc. of ICCV 2007. (2007) 1–7
8. Liu, X., Davis, B., Niethammer, M., Pizer, S., Mageras., G.: Prediction-driven respiratory motion atlas formation for 4d image- guided radiation therapy in lung. In: MICCAI'10 Pulmonary Image Analysis Workshop. (2010)
9. Cootes, T.F., Edwards, G.J., Taylor, C.J.: Active appearance models. IEEE Transactions on Pattern Analysis and Machine Intelligence **23**(6) (2001) 681–685
10. Segars, W., Lalush, D., Tsui, B.: Modeling respiratory mechanics in the mcat and spline-based mcat phantoms. Nuclear Science, IEEE Transactions on **48**(1) (feb 2001) 89 –97
11. Yushkevich, P.A., Piven, J., Cody Hazlett, H., Gimpel Smith, R., Ho, S., Gee, J.C., Gerig, G.: User-guided 3D active contour segmentation of anatomical structures: Significantly improved efficiency and reliability. Neuroimage **31**(3) (2006) 1116–1128